Contents

2 Detector and Physics Performance

The PPS forward proton measurement capability can enhance the ability of the CMS detector to carry out the primary physics program of the LHC in various sectors and extensions of the SM. This includes QCD processes in the exclusive gluon-guon channel, as well as electroweak physics in two-photon interactions. Discussion of the performance of the PPS tracking and timing detectors is presented, with the goal of estimating the sensitivity reach during the Run 2 data-taking period.

A brief description of the beam optics is provided in Sec. 2.1, occupancy and detector acceptance are presented in Sec. 2.2, followed by the extrapolation of the machine-induced background in Sec. 2.4. Finally, measurements and sensitivity reach for two reference physics processes are discussed in Sec. 2.6.

2.1 Beam optics

The configuration of the LHC beamline around the CMS interaction point (IP) is shown in Fig. 3 for the positive side (z>0). The proposed forward detector tracking and timing detector stations are to be installed in the regions located at approximately z=204 m and z=215 m from the IP in both beam directions downstream of the central detector. Protons that have lost energy in the primary interaction emerge laterally after passing through the bending magnets. At 204 m (215 m) one can observe protons that have lost a few percent ($\simeq 3-10\%$) of the initial beam energy.

Particle transport of the beamline is performed with HECTOR [36], which is incorporated in the CMSSW detector simulation and reconstruction package. Results are found in good agreement with MAD-X [37], the standard LHC beam transport program used at CERN. The HECTOR package tracks protons (or other particles) that emerge in the forward direction from the interaction region through the LHC beam pipes. The model of the LHC beamline is implemented, and the collimators and the apertures of the beamline elements are taken into account. If required, the beam transport can be updated for different optics configurations. Protons are generated with a "particle gun" Monte Carlo simulation that takes into account the energy loss and the four-momentum transfer at the vertex position. A proton beam energy of 6.5 TeV with appropriate LHC optics is used. Version 6.503 of the LHC optics files is used, with an emittance $\beta^* = 0.55$ m, an angular divergence $\sigma_\theta = 30.2$ μrad at the IP, a crossing angle =142.5 μrad in the horizontal plane, and a beam energy spread $\sigma_E = 0.77$ GeV. Full details can be found in Ref. [36]. **(to be checked ???)**

The beam profile is shown in Fig. 4 for the locations corresponding to the tracking and timing detector stations, at distances from the IP of z=203.8 m, 215.0 m, and z=215.5 m, respectively.

2.2 Occupancy and detector acceptance

The position and direction of the protons in the 204 m and 215 m detectors (for a given LHC optics) depend on the energy and scattering angle of the outgoing proton, as well as the vertex position and angle of the collision. The energy and scattering angle are directly related to the kinematic variables ξ, the fractional longitudinal momentum loss of the outgoing proton, and $|t|$, the square of the four-momentum transfer.

The dimensions of the PPS detectors (both timing and tracking) are constrained by the allocated space in the RP, and eventually determine the coverage in t, ξ. Particles with fixed values of $(|t|, \xi)$ propagated to the PPS detector location arrive at the X,Y positions shown in Fig. 5. They form ellipses due to the quadrupole magnets, with centers at $y = 0$. From this figure one can estimate the acceptance for any

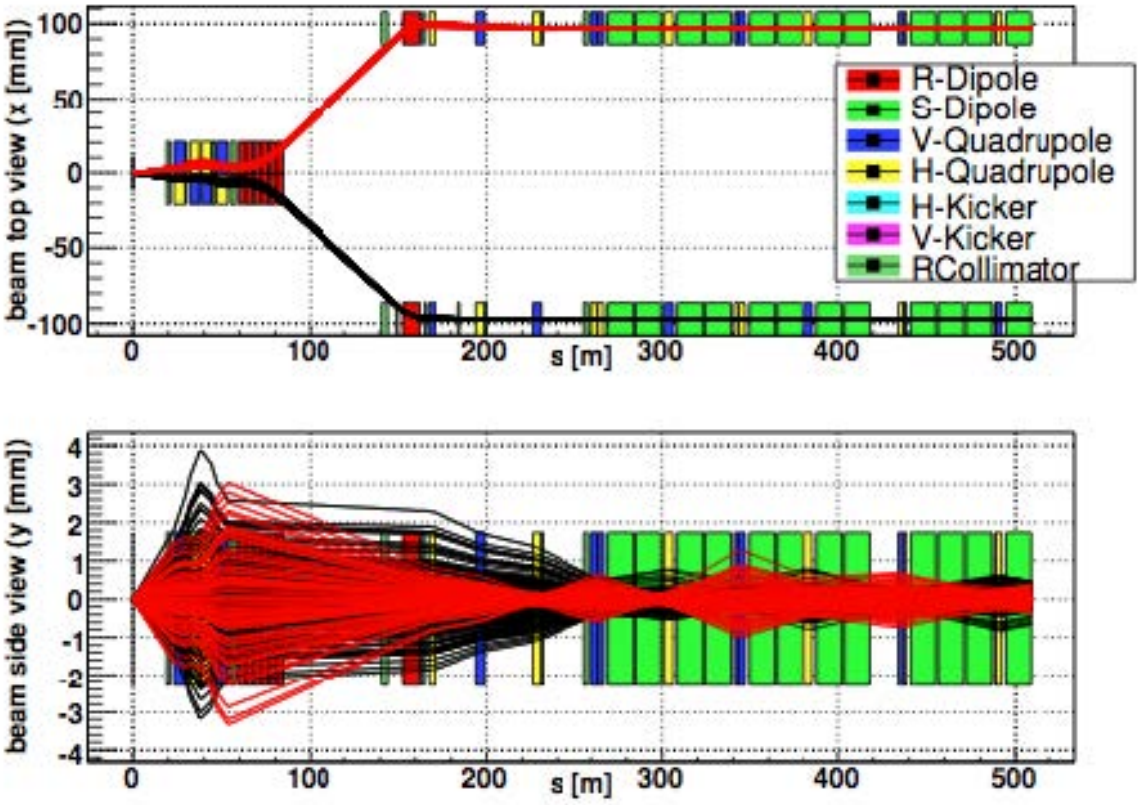

Figure 3: Top and side views of the beamline on the positive side (z>0) of IP showing the proton trajectories using HECTOR, a fast simulator for particle transport in the beamline. Here, the horizontal curvature of the beamline has been straightened out for the purpose of simplification.

detector coverage for a given t, ξ, as the fraction of the corresponding ellipse covered. The rectangle drawn by a dashed (solid) black line illustrates the boundaries of a detector with an area (in X, Y) of 20×18 mm^2 (**to be fixed???**) located at 15σ (20σ) from the beam center, whereas the beam dimensions are schematically drawn by circles.

In order to study the detector occupancy and acceptance for a given physics process, dedicated samples of exclusive dijet and WW events have been used, produced in gluon-gluon fusion and photon-photon interactions, respectively. Here (and in the following), the term "exclusive" refers to the production of a particular process (in this case, dijets or WW) without "anything else" coming from the primary hard interaction. In the absence of additional interactions, large "rapidity gaps", i.e. regions in pseudorapidity devoid of particle production, are expected around the exclusively centrally produced system. In both cases, the central systems of dijets or WW are required to be produced with rapidity $|y| < 2$. The ExHuME [39] signal generator is used to simulate exclusive dijet events, while the FPMC generator [38] is used to simulate exclusive WW events from the process $pp \rightarrow pWWp$. Beam energy dispersion and crossing angle including the smearing due to the beam divergence, vertex smearing, and detector resolution effects are accounted for. The presence of multiple interactions (pileup) per bunch crossing is incorporated by simulating additional interactions (both in-time and out-of- time with the collision) with a multiplicity of $\mu = 50$ matching that expected during Run 2.

Reconstruction of the kinematic variables is performed to measure the values of t and ξ, and determine their resolution. Reconstructed and generated values of t and ξ are shown in Fig. 6 and Fig. 7, respectively.

The particle hit distribution is studied for dimensions of the active area of the tracking detector stations

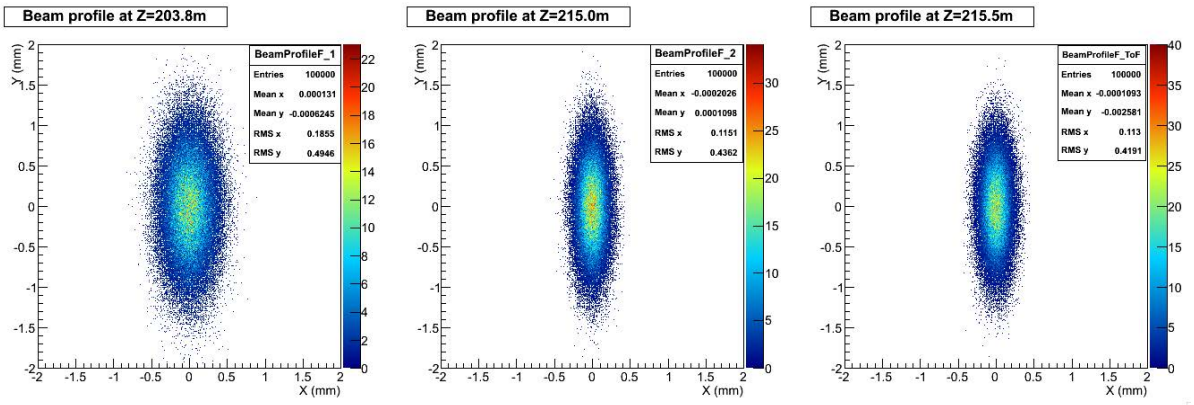

Figure 4: Beam profile in X and Y (in mm) at the z-positions corresponding to the two tracking stations (z=203.8 m and z=215.0 m) and to the time-of-flight detector (z=215.5 m).

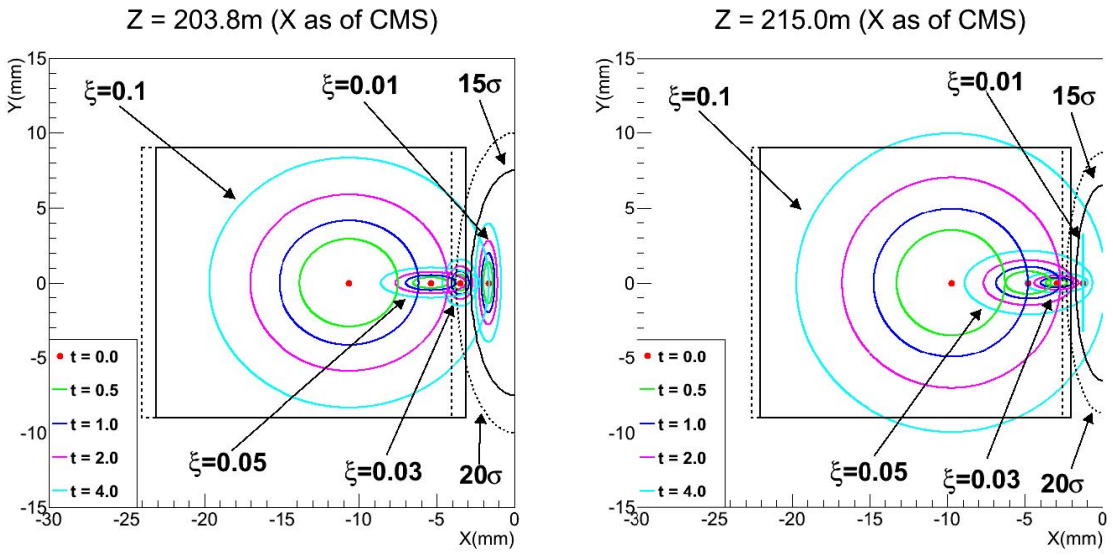

Figure 5: Particles with fixed t and ξ values propagated to the PPS detector position: $t - \xi$ ellipses for the protons at z=204 m (left) and z=215 m (right). The dashed (solid) black rectangle illustrates the detector dimensions at 15σ (20σ) from the beam center. The beam dimensions are also shown by circles. A "particle-gun" simulation based on HECTOR is used to generate protons at different (t, ξ, ϕ) values.

at 204 m and 215 m, where planes with an area of 12×15 mm^2 (in X, Y) are orthogonal to the beam direction. Detector segmentation is not implemented in the simulation, as tracking detectors are expected to have a finely segmented active area (pixel size in X,Y is $\approx 100 \times 150$ μm^2). The corresponding resolution is assumed in the smearing of the proton reconstruction position. Figure 8 shows the single-arm acceptance in the two-dimensional $(\xi, |t|)$ plane, when hits are required in both tracking stations (at z=204 m and z=215 m). The acceptance is estimated using a sample of exclusive WW events when the tracking detectors are placed at 15 σ (left) and 20 σ (right) from the beam center. An acceptance of approximately 39% is estimated when the protons are within the PPS detector geometrical acceptance.

Similar two-dimensional acceptance distributions in the $(\xi, |t|)$ plane are shown in Fig. 9 for a double-arm acceptance, i.e. when hits in the tracking stations on both sides of the IP are required. An acceptance of approximately 11% is estimated when the protons are within the PPS detector geometrical acceptance.

Single-arm and double-arm acceptances in the $(\xi, |t|)$ plane for exclusive dijet produced with the ExHuME signal generator are shown in Fig. 10 and Fig. 11, respectively. The acceptance is shown for a distance of the tracking detectors at 15σ (left) and 20σ (right) from the beam center. A single-arm

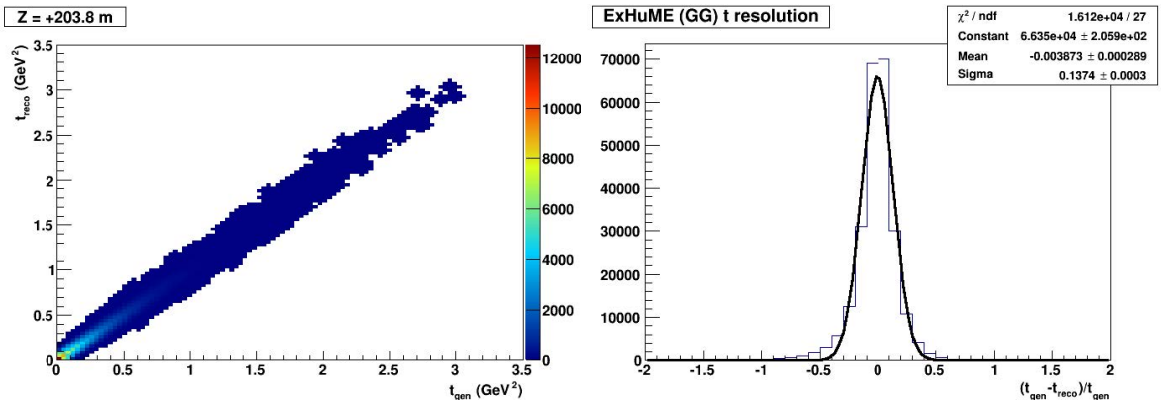

Figure 6: *Left:* Generated vs. reconstructed value of t for the protons within the PPS detector acceptance ($0 < |t| < 4, 0.01 < \xi < 0.2$). In the reconstruction, smearing effects due to vertex position, beam divergence and momentum are accounted for. *Right:* Resolution of the reconstructed t measurement, $(t_{reco} - t_{gen})/t_{gen}$. The ExHuME signal generator is used to simulate exclusive dijet events. The acceptance is shown for a distance of the tracking detectors at 15σ from the beam center.

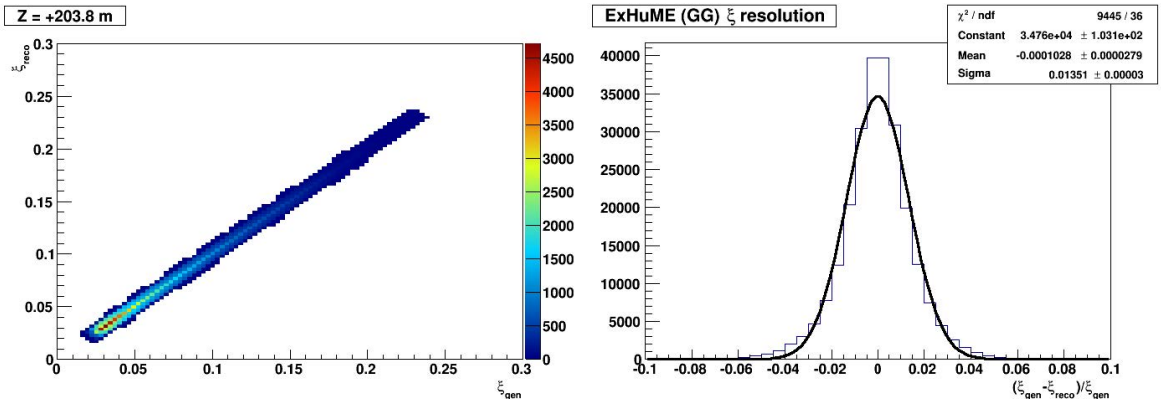

Figure 7: *Left:* Generated vs. reconstructed value of ξ for the protons within the PPS detector acceptance ($0 < |t| < 4, 0.01 < \xi < 0.2$). In the reconstruction, smearing effects due to vertex position, beam divergence and momentum are accounted for. *Right:* Resolution of the reconstructed ξ measurement, $(\xi_{reco} - \xi_{gen})/\xi_{gen}$. The ExHuME signal generator is used to simulate exclusive dijet events. The acceptance is shown for a distance of the tracking detectors at 15σ from the beam center.

(double-arm) acceptance of approximately 49% (7%) is estimated when the protons are within the PPS detector geometrical acceptance.

Occupancy of the time-of-flight detectors are also studied for different detector geometries (Fig. 12). Segmentation of the timing detector active area is considered for both the baseline option of the QUARTIC detectors, and for the study-option of "diamond-like" detectors. The QUARTIC geometry is constrained by the minimal transversal dimensions (due to the machining of the detector bars) and by the outgoing proton direction/angle, as each particle must be contained within the same detector bar in order to maximize the signal yield and minimize the cross-talk between neighboring bars. On the other hand, the "diamond-like" segmentation offers a flexible geometry by allowing the optimization of the detector occupancy depending on the distance from the beam center, thus reducing the occupancy rates closer to the beam. In the simulation, each L-shaped QUARTIC bar has the same X-Y transversal section of 3×3 mm^2; the "diamond-like" strips have a Y-dimension of 5 mm, with a variable width (in X) varying from 0.3 mm (closer to the beam) up to 4.6 mm (further away) depending on the distance from the beam. Multiple hits in the same cell would "blind" the detector functionality, and therefore the time-of-flight information cannot be used for rejecting pileup events. Such events are rejected from the data analysis,

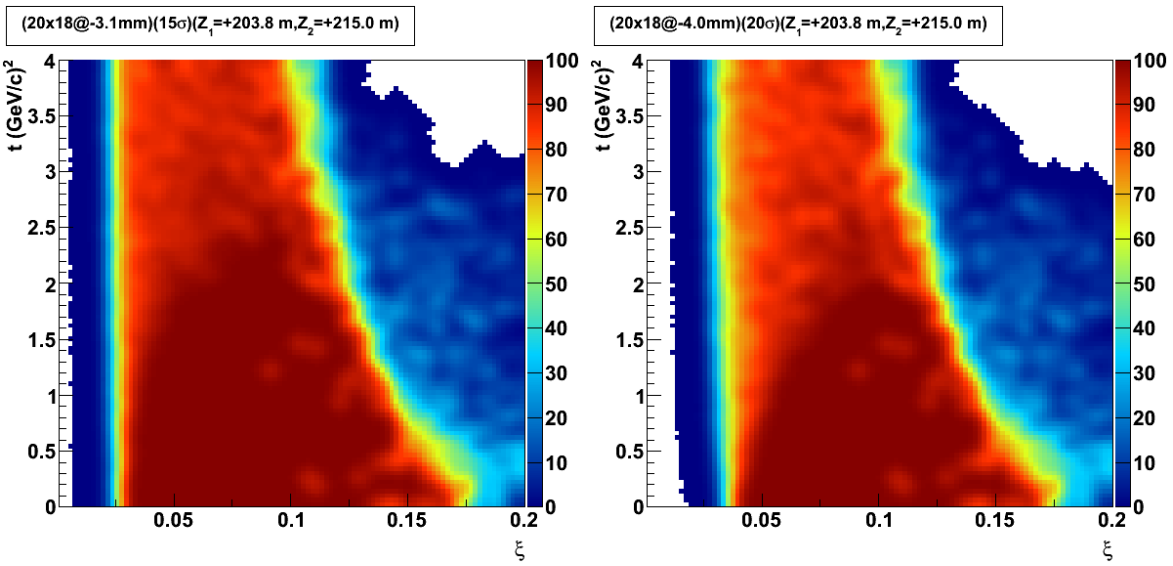

Figure 8: Acceptance in the $(\xi, |t|)$ plane for events in a single PPS arm, when requiring the coincidence of hits in the tracking stations at 204 m and 215 m only on one side of the IP. The FPMC signal generator is used to simulate $pp \to pWWp$ exclusive events. The acceptance is shown for a distance of the tracking detectors at 15σ (left) and 20σ (right) from the beam center. Pileup events are not included.

thus causing a source of inefficiency.

2.3 Mass acceptance and resolution

The acceptance and the achievable experimental resolution of the forward detectors depends ultimately on the LHC beam optics and on the position of the PPS detectors relative to the beam.

The acceptance as a function of the mass of a central system produced is shown in Fig. 13. Central exclusive dijet (left) or WW (right) events are studied. The acceptance is estimated for a distance of the tracking detectors of 15σ and 20σ from the beam center. In the estimate of the acceptance, an additional "dead" space of 0.3 mm between the active detectors and the beam position center is included to account for the window that separates the detectors from the vacuum of the beampipe. With detectors at 15σ from the beam, the PPS selects exclusive systems with masses in the 400-1600 GeV range, with an acceptance of at least 10%. The lower mass reach is strongly dependent on the distance of closest approach of the detectors. In general, both stations have larger acceptance for central systems in photon-photon than in gluon-gluon interactions (because of the smaller $|t|$). The distributions also show that the acceptance varies substantially with the distance of the tracking detectors from the beam. Operation of the detectors at 15σ (dashed lines in the plot) increases somewhat the acceptance for masses in the range of 400-700 GeV. Beam energy dispersion and crossing angle at the IP, and detector resolution effects are included in the estimate of the acceptance.

The mass is reconstructed with a resolution of approximately 2-3% from the generated mass of the produced system. Figure 14 shows the mass resolution estimated as a function of the mass of the centrally produced events in exclusive diet (left) and WW (right) events.

Figure 15 shows the hit distributions in the tracking detectors at z=204 m for exclusive dijet (left) and WW (right) events. The black squared lines schematically illustrate the X and Y dimensions (20×18 mm^2) of the detectors when placed at 15σ from the beam center. Detector and beam resolution effects are included in these plots.

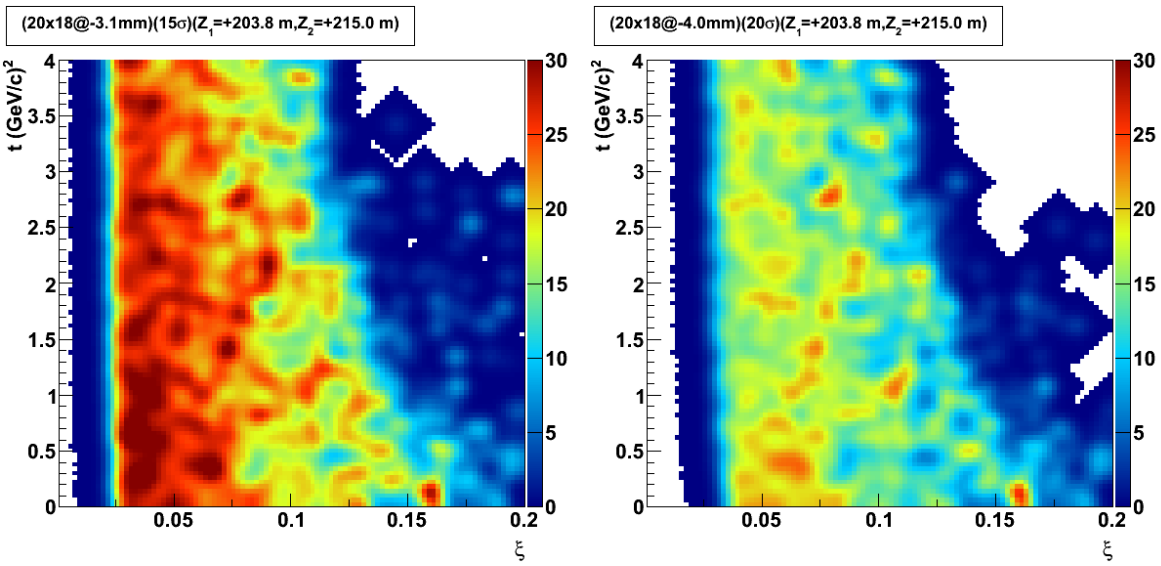

Figure 9: Acceptance in the $(\xi, |t|)$ plane for events selected in a double PPS arm, i.e. when requiring the coincidence of hits in the tracking stations at 204 m and 215 m on both sides of the IP. The FPMC signal generator is used to simulate $pp \to pWWp$ exclusive events. The acceptance is shown for a distance of the tracking detectors at 15σ (left) and 20σ (right) from the beam center. Pileup events are not included.

2.4 Instrumental backgrounds

In addition to the genuine physics processes from the hard interaction or from pileup events, instrumental background due to beam-gas interaction or any other "machine-induced" background must be estimated and included in the simulation.

The machine-induced background contribution at z=204-215 m is estimated by extrapolating the measurements by the TOTEM Roman Pot detectors, in the same location and with real data during the 2010-2012 proton-proton run, to the new beam intensity and data-taking conditions expected for Run 2. In particular, the track multiplicity measured in data during the Run 1 TOTEM data-taking periods with a number of pileup interactions of $\mu \simeq 9$ is compared with simulation (Fig. 16), and is extrapolated to the expected conditions of Run 2 with $\mu = 50$. In order to select debris remnants due to instrumental background (instead of those from genuine diffractive events), a coincidence of track segments (hits) reconstructed in the RP and T2 TOTEM stations on the "same-side" of the IP is required. These results are used to extract the scale factors to be applied to a simulation with $\mu = 50$, and extrapolate the tracking multiplicity for the expected Run 2 conditions.

2.5 RP alignment

2.6 Physics processes

Study of physics processes with forward protons may extend the physics reach of the LHC experiments. Here, we study two physics cases which address different issues: exclusive dijet and exclusive WW production. These processes will allow us to investigate central exclusive production with both protons measured in the mass region above 200 GeV, as well as to learn about rates, backgrounds, and operational aspects of the forward detectors. Knowledge already gained in operating the TOTEM experiment during Run 1, and the experience of combined CMS-TOTEM data-taking will be used. The exclusive dijets produced in gluon-gluon fusion will allow to test the theory of exclusive QCD physics. These jets are predicted to be nearly 100% gluon jets with a small admixture of $b\bar{b}$. The more rare high-energy two-

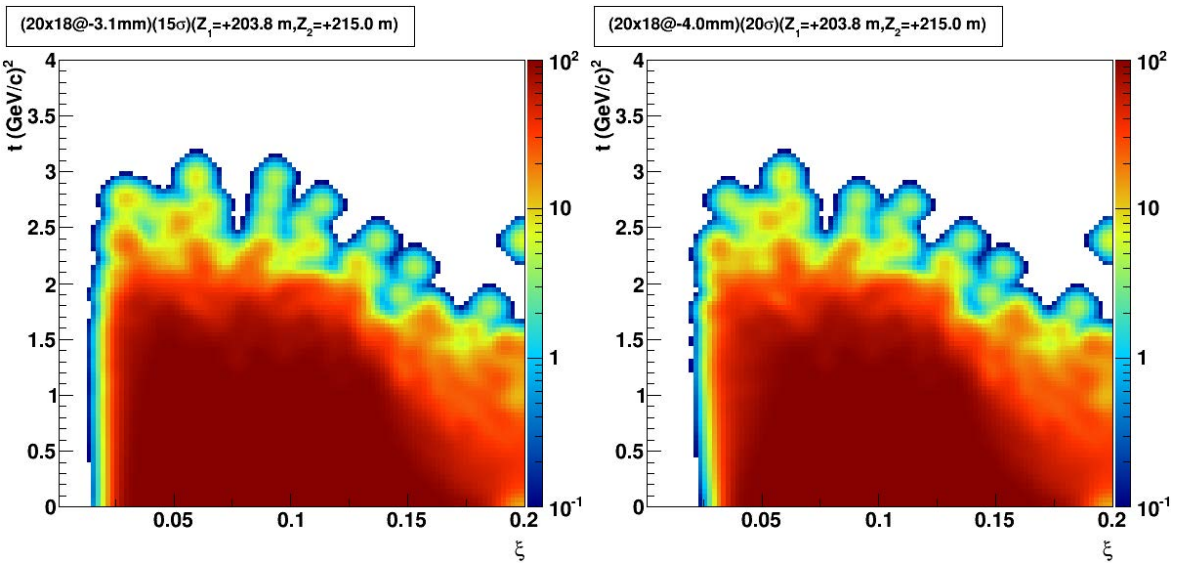

Figure 10: Acceptance in the $(\xi, |t|)$ plane for events in a single PPS arm, when requiring the coincidence of hits in the tracking stations at 204 m and 215 m only on one side of the IP. The ExHuME signal generator is used to simulate exclusive dijet events. The acceptance is shown for a distance of the tracking detectors at 15σ (left) and 20σ (right) from the beam center. Pileup events are not included.

photon exclusive production of $\gamma\gamma \to WW$ will extend the possibility to study quartic gauge-couplings as well as to study deviations from the expected $\gamma\gamma$ mass spectrum due to possible new BSM particle production. Schematic leading-order diagrams of these two processes are shown in Fig. 18.

2.6.1 Central exclusive dijet production

Exclusive dijet production in proton-proton collisions is a process in both protons escape the IP intact and a two-jet system is centrally produced $pp \to p'jjp'$. This process is a particular case of dijet production in Double Pomeron Exchange (DPE), a diffractive process in which the protons suffer a small fractional momentum loss, and a system X containing two jets is produced, $pp \to (p'IP)(p'IP) \to p'Xp'$. The Pomeron $\mathbb{P}$ is an exchange consisting of a colorless combination of gluons and/or quarks carrying the quantum numbers of the vacuum. Dijet production in DPE is a sub-process to dijet production in single-diffraction (SD) dissociation, where only one proton survives while the other dissociates. A schematic diagram for DPE dijet production is shown in Fig. 18 (left). Dijet production in DPE may occur as an exclusive process with only the jets in the final state, and no Pomeron remnants. In a special case, exclusive dijets may be produced through an intermediate state of a Higgs boson decaying into $b\bar{b}$. Exclusive production may also occur through a t-channel two-gluon exchange at leading order in perturbative QCD as shown schematically in Fig. 18 (left). Exclusive dijet production was first observed at the Tevatron [40] in hadronic collisions. A first study of dijet production at $\sqrt{s} = 7$ TeV is presented in Ref. [41]. In addition to providing information on QCD aspects of vacuum quantum number exchange, there is currently intense interest in using measured exclusive dijet production cross sections to calibrate theoretical predictions for exclusive Higgs boson production at the LHC. Such predictions are generally hampered by large uncertainties due to non-perturbative suppression effects associated with the rapidity gap survival probability. As these effects are common to exclusive dijet and Higgs boson production mechanisms, dijet production potentially provides a standard candle process against which to calibrate the theoretical models. Furthermore, any centrally produced system of mass X may appear as en excess over background expectations. With the addition of the PPS as "proton taggers", a significant enhancement of the sensitivity to these physics processes may be reached.

no results yet in this channel

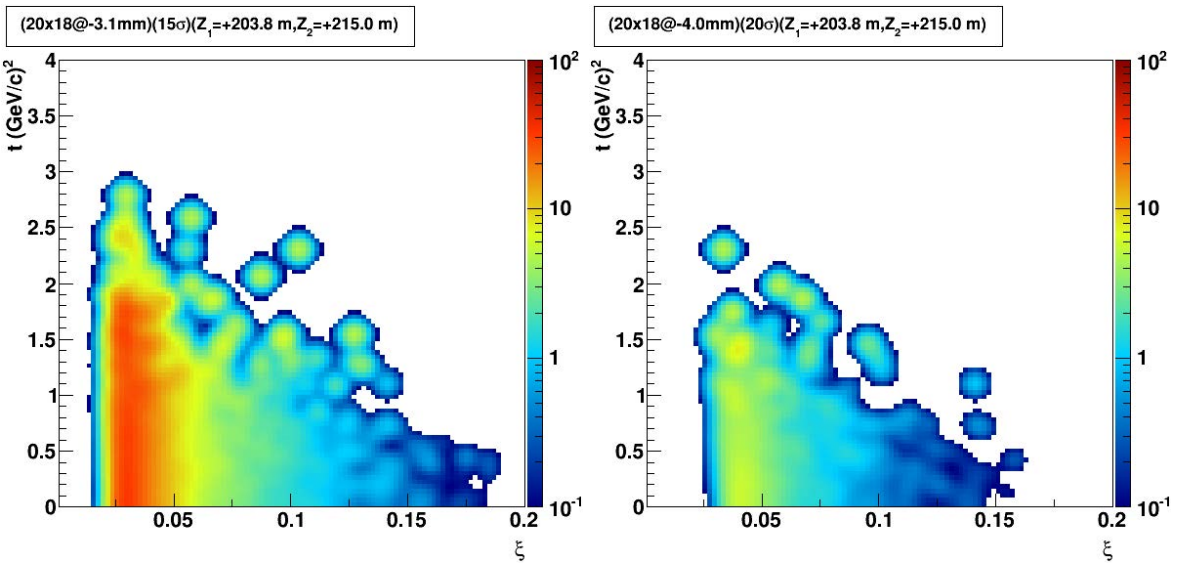

Figure 11: Acceptance in the $(\xi, |t|)$ plane for events in a single PPS arm, when requiring the coincidence of hits in the tracking stations at 204 m and 215 m on both sides of the IP. The ExHuME signal generator is used to simulate exclusive dijet events. The acceptance is shown for a distance of the tracking detectors at 15σ (left) and 20σ (right) from the beam center. Pileup events are not included.

2.6.2 Central exclusive WW production

Study of high-energy photon interactions at the LHC opens up the possibility of interesting and novel research [42, 43]. In particular, measurements of the two-photon production of a pair of W-bosons provide sensitivity to anomalous quartic gauge couplings of the gauge bosons. Measurements of the exclusive two-photon production of muon and electron pairs, in the process $pp \to p\ell^+\ell^- p$, were performed using 5.05 fb^{-1} of data collected in proton-proton collisions at $\sqrt{s} = 7$ TeV with the CMS detector at the LHC in 2011 [44]. Model-independent upper limits were extracted and compared to predictions involving anomalous quartic gauge couplings.

The current study is based on the experimental techniques developed in Ref. [44] and is intended to explore the potential sensitivity reach of the PPS detector. With the integrated luminosity expected to be collected during Run 2 and with the upgraded PPS detectors used in combination with the CMS central detector, the experimental reach can be extended by several orders of magnitude with respect to the best limits obtained so far.

In the process $pp \to pWWp$, both forward-scattered protons are detected in the PPS detectors, depending on the acceptance of the mass of the WW central system produced (Fig. 13). Such a production process is characterized by a primary vertex from a $\ell^\pm\ell^\mp$ (where $\ell = e, \mu$) pair with no other tracks, with large transverse momentum of the dilepton system, $p_T(\ell^\pm\ell^\mp)$, and large invariant mass, $M(\ell^\pm\ell^\mp)$.

A sample of 8k exclusive $pp \to pWWp$ events is used, and only the $\mu\mu$ final state is selected. The dominant backgrounds come from inclusive production of W^+W^- and $\tau^+\tau^-$ pairs. The sample of 8k events corresponds to an integrated luminosity of approximately 800 fb^{-1}.

The simulated samples for the signal process are compared to the SM expectation for the backgrounds. Tails of the $p_T(\ell^\pm\ell^\mp)$ distribution, where the SM $\gamma\gamma \to W^+W^-$ contribution is expected to be small, are investigated to look for anomalous quartic gauge couplings.

Events are selected by requiring two leptons of opposite charge, with a minimum transverse momentum $p_T > 20$ GeV, above the trigger threshold. In order to reduce the contamination from the W+jet (or other non-prompt lepton) background, "tight" lepton identification criteria are required (as in Ref. [44]).

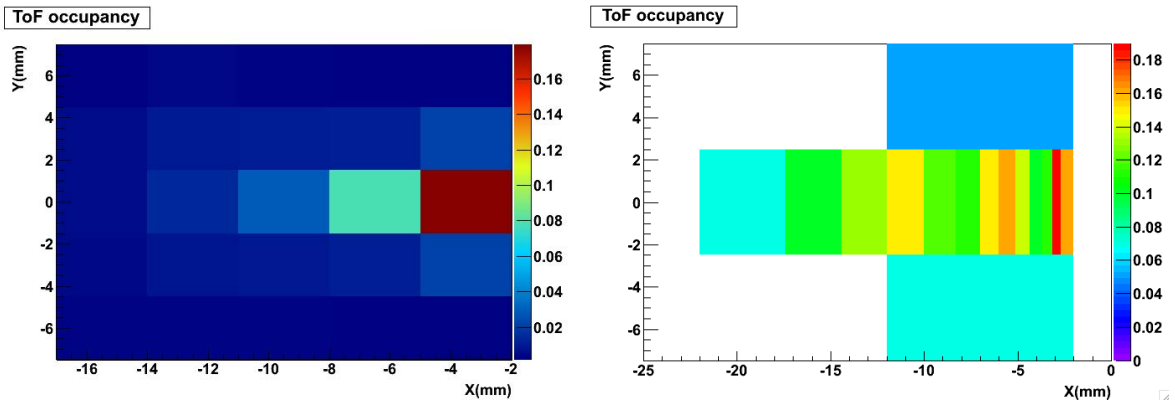

Figure 12: Detector occupancy of the time-of-flight detectors (at z=215.5 m) with a segmentation corresponding to QUARTIC (left) or diamond-like" (right) geometries. Smearing effects due to vertex position, beam divergence and momentum are accounted for. Particles are generated the FPMC signal generator to simulate exclusive WW events, and 50 pileup interactions are superimposed on the primary interaction.

Protons in the PPS detector acceptance are also expected, and the presence of hits in both tracking and timing detectors is therefore required. Finally, a correction due to the instrumental background from additional sources (as discussed in Sec. 2.4) is applied. Table 1 summarizes the event yields after each selection cut, the relative cumulative efficiency, and the expected cross section (including the branching fraction).

Table 1: Number of expected signal events, relative cumulative efficiency, and cross section times branching fraction ($\sigma \times \mathcal{B}$) after each selection cut, for a sample of 8k exclusive WW events, corresponding to an integrated luminosity of approximately 800 fb^{-1}. Only the $\mu\mu$ final state is considered. Statistical uncertainties are shown.

Selection	Events	Relative cumulative efficiency	$\sigma \times \mathcal{B}$ (fb)
generated WW events	1938$\pm$ xx	100%	0.8
both muons within geometrical acceptance ($\eta < 2.4$)	1335$\pm$ xx	69%	0.57
both muons reconstructed ($p_T > 20$ GeV)	960$\pm$ xx	49%	0.41
opposite charge muons, "tight" identification	807$\pm$ xx	42%	0.35
protons in PPS detectors (timing and tracking)	62$\pm$ xx	3.2%	0.025
no overlapping background hits in timing detectors	34$\pm$ xx	1.8%	0.014

Information of the protons time-of-flight arrival to the PPS detectors can be used as additional background rejection. After requiring coincidence of hits in both tracking and timing detector stations, the time-of-flight information is shown in Fig. **??** as a function of the z-vertex position of the leading central muon. Absolute arrival time of the leading protons at either positive ($z > 0$) and negative ($z < 0$), and the time-of-flight difference between both positive and negative detector arms. A timing resolution of 10 ps is assumed.

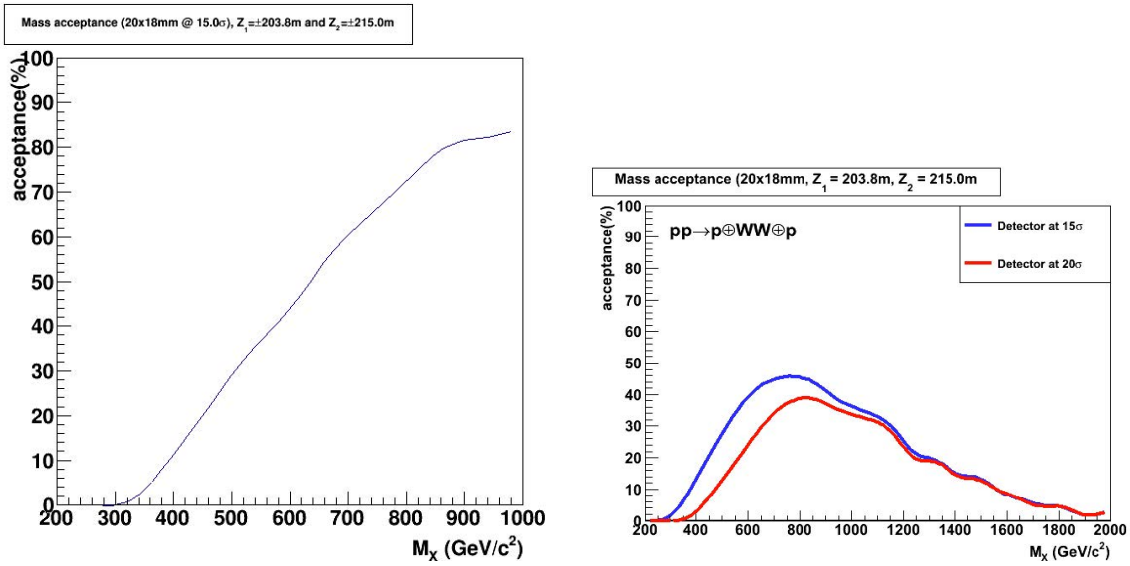

Figure 13: Mass acceptance as a function of centrally produced mass for exclusive diet events produced in gluon fusion (left, computed with ExHuME), and exclusive WW events produced in photon-photon processes (right, computed with FPMC). In the simulation, a coincidence of the tracking detectors placed at 204 m and 215 m is required. The estimated acceptance is shown as a solid (dashed) line when the tracking detectors are located at a distance of 15 (20) σ from the beam center.

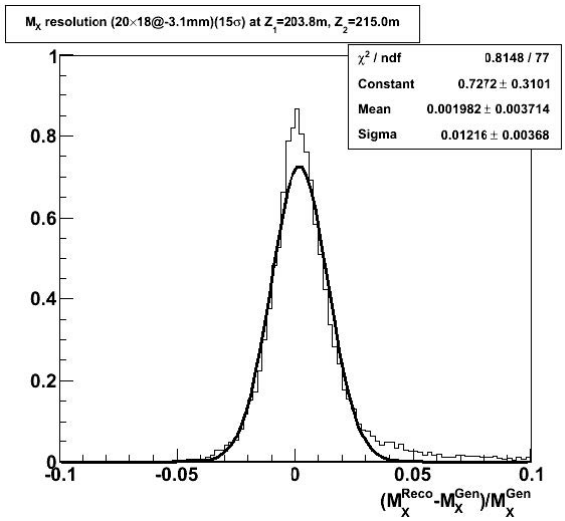

Figure 14: Mass resolution as a function of the mass of the centrally produced events in exclusive dijet (left) and WW (right) events. The estimated resolution is shown for tracking detectors located at a distance of 15 σ from the beam center.

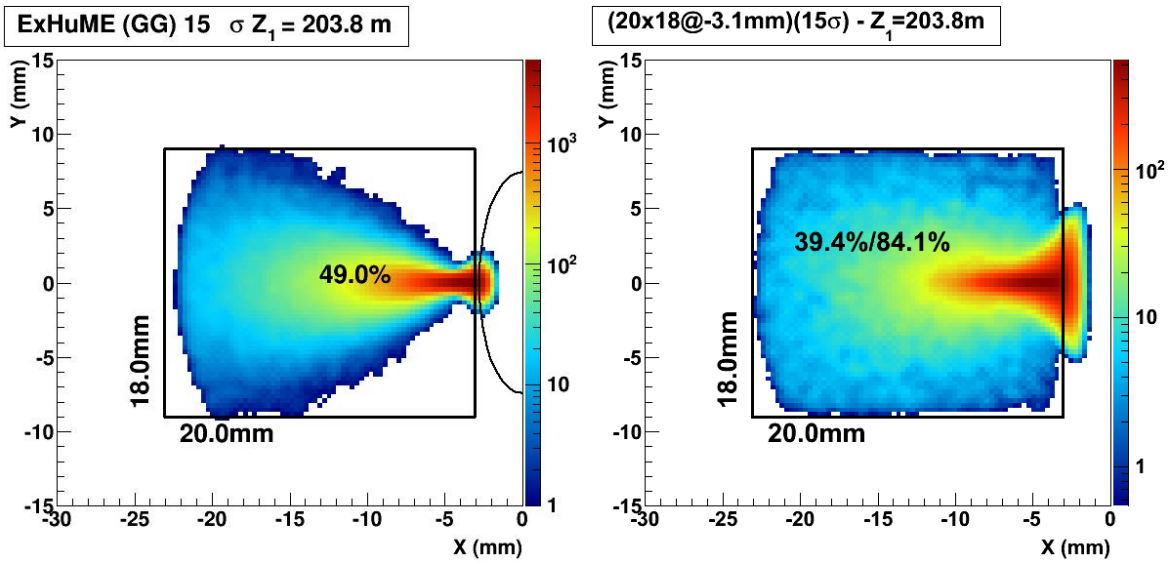

Figure 15: Hit distributions for centrally produced exclusive dijet (left) and WW (right) events are shown for the tracking detectors located at z=204 m. The black squared line schematically illustrates the boundaries of the tracking detectors in X and Y, when located at 15σ from the beam center. Beam energy and vertex smearing, and detector resolution are accounted for.

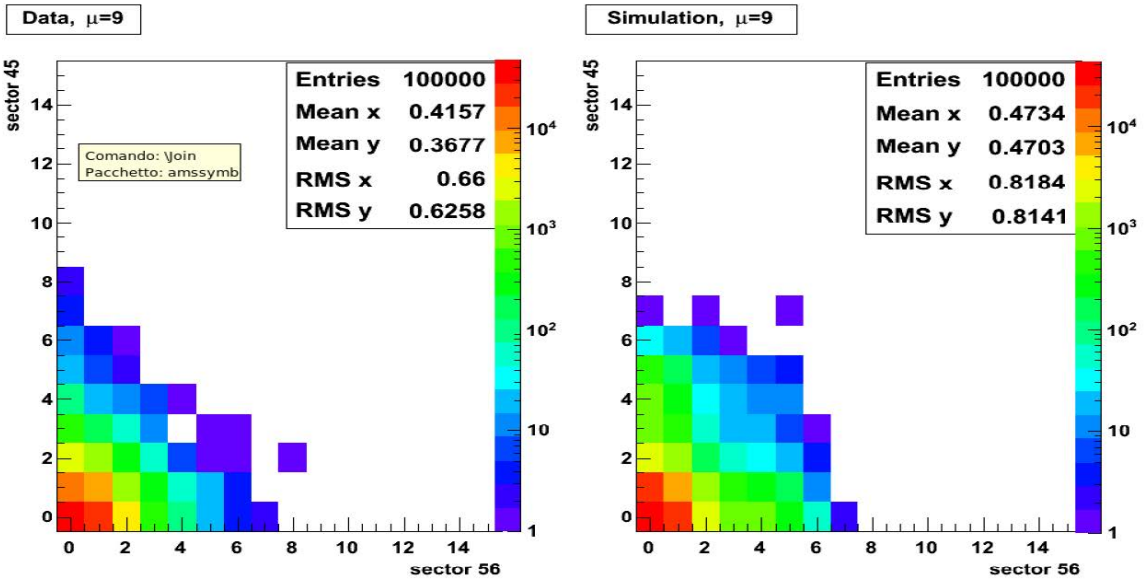

Figure 16: Track multiplicity in data (left) and simulation (right) for the Run 1 TOTEM data-taking period with a number of pileup interaction $\mu \simeq 9$. These results are used to extract the scale factors to be applied to a simulation with $\mu = 50$, and extrapolate the tracking multiplicity for the expected Run 2 conditions.

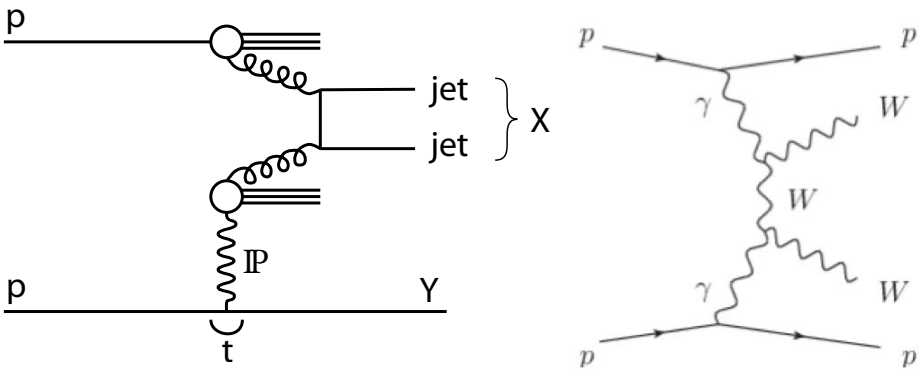

Figure 17: Leading order diagrams for exclusive dijet (left) and exclusive WW (right) production in pp collisions.

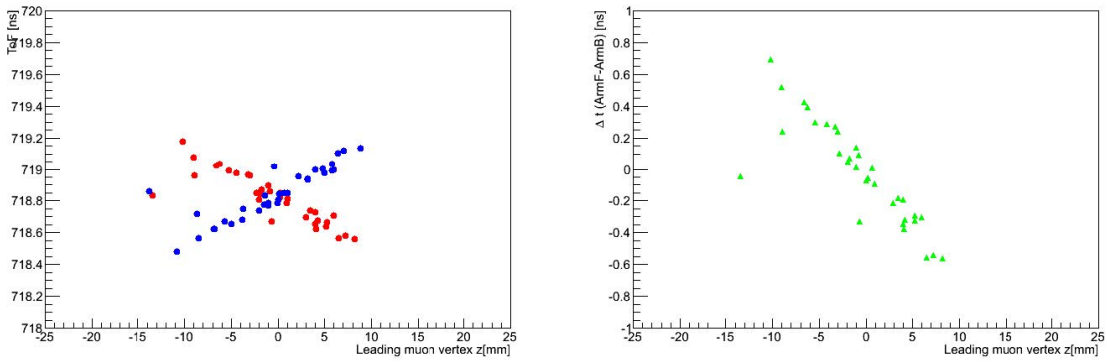

Figure 18: Absolute arrival time of the leading proton at positive and negative detector arms (left), and corresponding time-of-flight difference (right). A timing resolution of 10 ps is assumed. Simulation is shown for a sample of exclusive WW events.